npj | clean water

www.nature.com/npjcleanwater

ARTICLE OPEN

Check for updates

Efficient removal of aromatic pollutants via catalytic wet peroxide oxidation over synthetic anisotropic ilmenite/carbon nanocomposites

Sheng Guo[1], Ran Huang[2], Jia Yuan[1], Rong Chen[1,3] and Fengxi Chen[1]✉

As one of the most common ferrous (Fe^{2+})-containing oxide minerals in the Earth's crust, ilmenite ($FeTiO_3$) is a potential low-cost heterogeneous Fenton-like catalyst for organic wastewater treatment via catalytic wet peroxide oxidation (CWPO). However, it suffers from low activity and long induction time. Herein anisotropic $FeTiO_3$/C nanocomposite with rich Fe^{2+} ions on large surface area of 159.0 $m^2\ g^{-1}$ (surface Fe/Ti and Fe^{2+}/Fe^{3+} ratios were respectively 2.1 and 2.0) was prepared via cetyltrimethylammonium (CTA^+)-assisted sol-gel synthesis. CTA^+ modulated the growth of $FeTiO_3$ nanoparticles with more exposed metallic sites by preferential adsorption on its (104) plane via electrostatic attraction, provided the carbon source and facilitated the generation of more Fe^{2+} ions at the interface of $FeTiO_3$/C via carbothermal reduction of $FeTiO_3$. $FeTiO_3$/C efficiently catalyzed CWPO removal of six aromatic pollutants with different charges (25 mg L^{-1} each) at 25 °C and pH 3.0 without an induction period owing to rich Fe^{2+} content on neutral surface (pH_{pzc} ~3.3)—three dye solutions completely decolorized in 1 h and three antibiotics degraded by >90% in 3 h. Reusability of $FeTiO_3$/C was demonstrated with cationic rhodamine B and anionic orange G dyes in five consecutive runs. Scavenging tests and spin-trapping EPR spectra confirmed the generation of dominant ·OH and minor $O_2^{\bullet-}$ species for organic degradation via catalytic decomposition of H_2O_2 on $FeTiO_3$/C as a heterogeneous Fenton-like catalyst.

npj Clean Water (2023)6:74; https://doi.org/10.1038/s41545-023-00287-1

INTRODUCTION

Recalcitrant aromatic compounds (e.g., ionic dyes and pharmaceuticals shown in Table 1) constitute a major type of organic pollutants in wastewater. Ionic dyes are extensively used in textile, paper, leather, personal care and food processing industries[1], whereas emerging pharmaceutical pollutants such as tetracycline and metronidazole are indispensable antibiotics in daily life. Their untreated effluents are not only aesthetically undesirable, but also harmful to water users due to potential CMR or other chronic biological effects (CMR for carcinogenicity, mutagenicity and toxicity for reproduction).

Various treatment technologies (physical, biological or chemical) have been explored to remove aromatic pollutants. Among these, physical adsorption only transfers toxic pollutants from solution to solid, which requires further treatment of contaminated adsorbents, and biological processes are not suitable for toxic or non-biodegradable pollutants. Therefore, catalytic wet peroxide oxidation (CWPO) has attracted wide attention for organic wastewater treatment[2,3]. In this aspect, most organic pollutants can be effectively degraded via Fenton oxidation, wherein hydroxyl radicals (•OH) with high redox potential (~2.80 V) are in-situ generated by ferrous ions (Fe^{2+})-catalyzed decomposition of H_2O_2 according to Eq. 1. However, the conventional Fenton process generates undesired iron sludge with high-color effluent since it uses soluble inorganic ferrous salts (e.g., $FeSO_4{\cdot}7H_2O$) as homogeneous catalysts. Therefore, many efforts have been devoted to the development of efficient heterogeneous Fenton-like catalysts for sustainable remediation of organic wastewater[2–4].

$$Fe^{2+} + H_2O_2 \rightarrow Fe^{3+} + \bullet OH + OH^- \quad (1)$$

Ilmenite ($FeTiO_3$) is one of the most common Fe^{2+}-containing oxide minerals in the Earth's crust[5–10]. Its catalytic applications have attracted much attention because of its good structural stability and low toxicity[11–13]. The Fe^{2+} ions in $FeTiO_3$ are expected to act as Fenton-like active species for catalytic decomposition of H_2O_2 to generate •OH via Eq. 1, which has been well demonstrated in other Fe^{2+}-containing oxides such as Fe_3O_4[14–19]. Therefore, with ~36.8 wt% of structural Fe^{2+} ions, ilmenite would be a potential earth-abundant, low-cost, active and stable heterogeneous Fenton-like catalyst[12,13]. However, its two main drawbacks in relation to a long induction period (e.g., a 3 h induction time in CWPO of phenol at pH 3 and 25 °C[12]) and low activity (e.g., slow decomposition rate of H_2O_2 at $(1–3)\times10^{-3}$ min^{-1} on natural ilmenite at pH 3 or 7)[3,20] seriously restrict its practical applications in CWPO. In addition, only limited model pollutants (usually phenol) have been used to assess the catalytic performance of $FeTiO_3$ while other pollutants remain largely unexplored so far.

Several methods have been developed to overcome the drawbacks of natural ilmenite. $FeTiO_3$-based CWPO processes were strengthened by increasing the reaction temperature—complete conversion of 100 mg L^{-1} phenol in 4 h with 71% of TOC removal after reacting with 500 mg L^{-1} H_2O_2 over 1 g L^{-1} $FeTiO_3$ at pH 3 and 75 °C[3]. However, high temperatures need more energy input and increase the process cost. Photo-assistance may improve the oxidation rates of CWPO processes based on $FeTiO_3$

[1]State Key Laboratory of New Textile Materials & Advanced Processing Technologies, Wuhan Textile University, 430200 Wuhan, PR China. [2]School of Chemistry and Environmental Engineering, Wuhan Institute of Technology, 430073 Wuhan, PR China. [3]Henan Institute of Advanced Technology, Zhengzhou University, 450002 Zhengzhou, PR China. ✉email: fxchen@wtu.edu.cn

Table 1. Chemical structures of six typical aromatic pollutants.

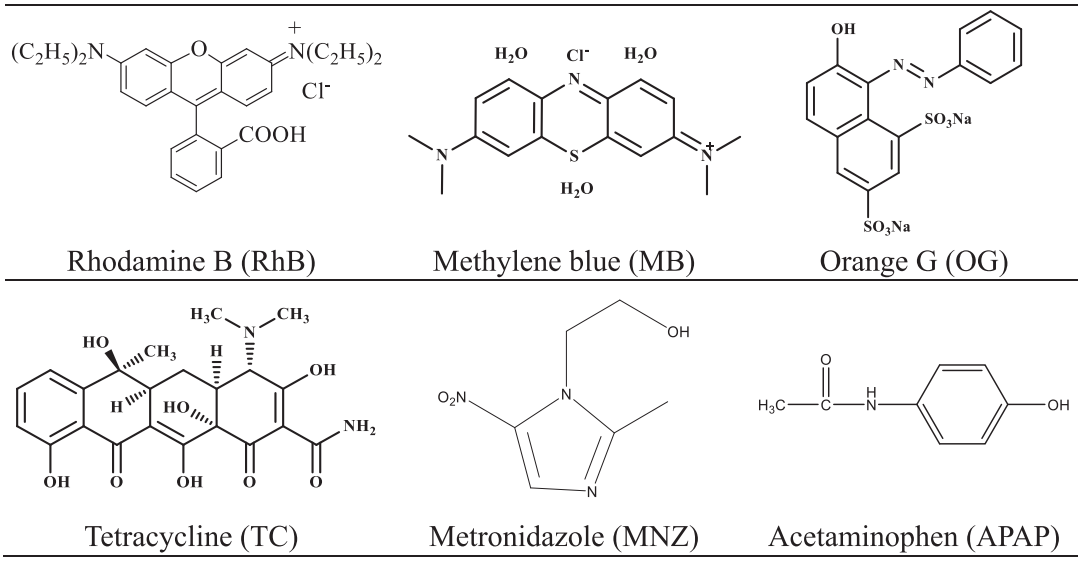

or its composite (e.g., $FeTiO_3/TiO_2$) via expediting redox cycling of Fe^{3+}/Fe^{2+} or by facilitating the generation of more reactive species (e.g., •OH or superoxide radicals ($O_2^{\bullet-}$))[3,12,13,21,22]. However, external light sources are required in photo-assisted CWPO, which still hinders the applications of $FeTiO_3$ on large scale. It was also reported that the decrease in iron oxidation state on the ilmenite surface improved its catalytic activity[13]. The amount of low-valent iron (Fe(II) and Fe(0)) on the surface increased upon reduction of raw ilmenite with H_2 in the temperature range of 25–1000 °C, which in turn increased the decomposition rate of H_2O_2 and generated more •OH radicals for higher oxidation rates of organic contaminants[13]. However, it is difficult to obtain $FeTiO_3$ with surface-enriched low-valent iron species without post-treatment due to their inherent instability under ambient conditions.

Synthetic $FeTiO_3$ particles can be prepared by solid-state reactions, hydrothermal syntheses and sol-gel methods. The products made via solid-state reactions (including mechanochemical milling) are usually impure or in homogeneous[21,23]. Hydrothermal syntheses of $FeTiO_3$ in closed autoclaves require high reaction temperature and high autogenous pressure with safety concern (e.g., 220 °C for 10 h[22,24,25]). In comparison, the sol-gel method is easier to perform[21,26–28], in which a gel precursor is first prepared by a sol-gel process, followed by thermal annealing at suitable conditions (e.g., 700 °C for 10 h in N_2[21], or 600 °C for 2 h in air[26]). In addition, some functional organic additives (e.g., polymers and surfactants) can be included into the gel precursor to adjust the particle size, morphology and homogeneity of the obtained $FeTiO_3$ after pyrolysis.

In this work, a cationic surfactant cetyltrimethylammonium (CTA^+) bromide (denoted as CTAB) was added during the formation of the gel precursor. CTAB is a well-known template for the synthesis of siliceous M41S-type mesoporous materials via interfacial self-assembly between CTA^+ and negatively charged siliceous species[29]. Herein CTAB was employed to modulate the growth of $FeTiO_3$ nanoparticles via preferential adsorption. To promote electrostatic interaction at the interface between inorganic species and CTA^+, it is critical to carry out the hydrolysis and condensation of iron and titanium sources under basic condition, which results in negatively charged inorganic species. The acidic condition used in the reference[26] (pH adjusted by HNO_3 to 1–2) led to positively charged inorganic species, which is not beneficial for its interaction with CTA^+ due to electrostatic repulsion. Triethylamine (TEA) was found to be a suitable organic base without introducing other metal impurities for the preparation of $FeTiO_3$ nanoparticles upon pyrolysis of the gel precursor at 700 °C. TEA has been used as a template for the synthesis of microporous aluminophosphate molecular sieves (e.g., AlPO4-5[30], SAPO-34[31,32]) or nanocalix Ln(12) clusters of diacylhydrazone[33]), as an etching agent for post-synthesis of hierarchical SAPO-34[34], or as a basic complexing agent for the formation of lanthanide (hydro)oxide nanorods[35,36]. In addition, CTAB serves as a carbon source upon pyrolysis to make $FeTiO_3/C$ nanocomposites. More importantly, in-situ generated carbon partially reduced Fe^{3+} to Fe^{2+} at the $FeTiO_3$/carbon interface at high temperature in N_2[37], which results in $FeTiO_3$ nanoparticles with rich Fe^{2+} ions on large surface area for enhanced activity in CWPO.

RESULTS AND DISCUSSION

Characterization of $FeTiO_3/C$ nanocomposites

Figure 1 showed the XRD patterns of samples made from different initial molar compositions of 1.0Fe : 1.0Ti : xCTAB : yTEA (x = 0, 0.67 or 1.33, y = 0 or 4.0). The sample obtained without the addition of TEA (denote as $FeTiO_3$/C-NT, NT for No TEA (y = 0)) to the initial reaction mixture contained only low-crystalline $FeTiO_3$ particles, as manifested by weak and broad peaks with low signal-to-noise ratio in Fig. 1d. At the fixed amount of TEA (y = 4.0), different $FeTiO_3/C$ samples prepared with varying concentrations of CTAB (denoted as $FeTiO_3$/C-x, x = 0, 0.67 and 1.33) exhibited similar XRD patterns (Fig. 1(a–c)). The peaks at 2θ = 23.8°, 32.4°, 35.3°, 40.3°, 48.7°, 52.8°, 61.5°, 63.3° and 70.1° were indexed to (012), (104), (110), (113), (024), (116), (214), (300) and (1010) diffractions, respectively, according to the standard pattern of $FeTiO_3$ (PDF #29-0733).

Some differences were discernable in Fig. 1(a–c). Firstly, a peak at 2θ = 27.5° appeared in the XRD pattern of $FeTiO_3$/C-1.33 (Fig. 1a inset), which was assigned to the (110) diffraction of rutile TiO_2 (PDF #84-1284). Due to higher CTAB concentration (~10 wt%) used in the synthesis of $FeTiO_3$/C-1.33, CTAB micelles were formed with some TBOT molecules solubilized in the hydrophobic micellar core, which led to the formation of separate TiO_2 phase as minor impurity in $FeTiO_3$/C-1.33. Secondly, the (012) and (110) peaks of

$FeTiO_3$/C-0.67 synthesized with lower CTAB concentration (~5 wt %) were intensified with regard to the (104) peak (I_{012}:I_{104}:I_{110} = 0.5:1.0:1.0 in Fig. 1b) while the relative XRD peak intensities in Fig. 1c for $FeTiO_3$/C-0, which was $FeTiO_3$ synthesized without the addition of CTAB, were very close to the standard diffraction data of $FeTiO_3$ (I_{012}:I_{104}:I_{110} = 0.3:1.0:0.7). This indicates larger growth rates of the (012) and (110) planes than that of the (104) plane in CTAB-assisted sol-gel synthesis of $FeTiO_3$/C-0.67, which was attributed to preferential adsorption of CTA^+ cations on the (104) plane of $FeTiO_3$.

To examine the adsorption of CTA^+ on different crystal planes of $FeTiO_3$, the $FeTiO_3$ lattice was cleaved along (104), (012) and (110) planes, respectively, using Materials Studio 7.0 (Fig. 2). The crystal structure of $FeTiO_3$ was imported from the reference. [38]. As displayed in Fig. 2a, the top layer of the cleaved (104) plane exclusively comprises lattice oxygen (O_L, O^{2-}) with the density of $5O_L$ per nm^2, which favors the adsorption of CTA^+ due to electrostatic attraction between CTA^+ and surface O^{2-}. Therefore, the growth of the (104) plane is restricted by the adsorbed CTA^+. In comparison, the top layer of the cleaved (012) plane has a lower O_L density ($3O_L$ per nm^2, Fig. 2b). As such, the growth of the (012) plane is less inhibited by the adsorbed CTA^+. On the other hand, the top layer of the cleaved (110) plane mainly contains metal (Fe and Ti) cations with atomic ratios of 2Fe:2Ti:1 O (Fig. 2c). The positively charged (110) top surface is unbeneficial for the adsorption of CTA^+ due to electrostatic repulsion. Therefore, the addition of CTA^+ has little impact on the (110) growth. The unhindered growth of the (110) plane exposes more metallic ions on the particle surface, which serve as active sites for the activation of H_2O_2 on $FeTiO_3$/C.

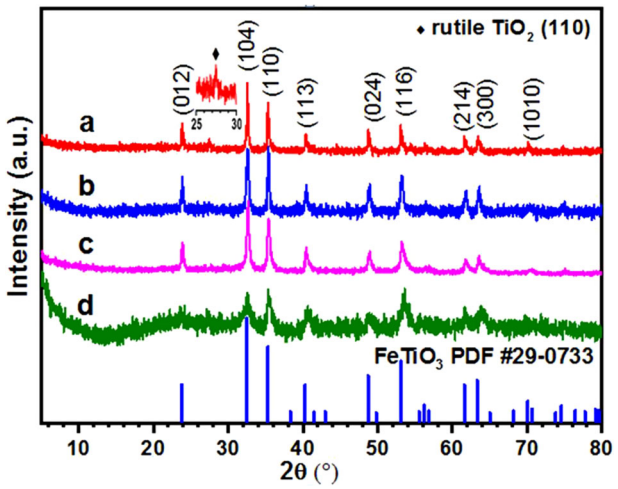

Fig. 1 XRD patterns of samples made from different initial molar compositions of 1.0Fe:1.0Ti:*x*CTAB:*y*TEA. **a** $x = 1.33$, $y = 4.0$; **b** $x = 0.67$, $y = 4.0$; **c** $x = 0$, $y = 4.0$ and **d** $x = 0.67$, $y = 0$.

In addition to modulating the growth of $FeTiO_3$/C-0.67, CTAB also serves as a carbon source by pyrolysis at 700 °C in N_2. The TG/DSC analysis of the gel precursor in N_2 (Fig. 3) revealed that it underwent mass loss in three stages. The first stage up to 145 °C lost 7.6% of the initial mass accompanied by a small endothermic peak at 98 °C in the DSC curve, which was mainly attributed to the loss of residual ethanol and water in the precursor. In the second stage from 145 °C to 200 °C, 35.6% of mass loss was recorded accompanied by an exothermic peak at 190 °C in DSC, which was mainly due to partial crystallization of inorganic iron/titanium components. The last stage up to 700 °C (23.4% loss in mass) may involve some overlapped processes, e.g., endothermic decomposition of organic residues and exothermic crystallization of inorganic components. The superposition of different processes made the overall thermal effect very weak. No obvious change in mass was observed after 700 °C, implying complete conversion of the gel precursor to $FeTiO_3$/C.

The carbon content in $FeTiO_3$/C was determined by EDX to be 11.5±1.9 wt% (Fig. 4a). The characteristic D band at 1350 cm^{-1} (disordered carbon) and G band at 1588 cm^{-1} (graphitic carbon) were observed in the Raman spectrum of $FeTiO_3$/C (Fig. 4b)[39–42]. The large area ratio of D to G band (A_D/A_G: 3.5) indicates the existence of abundant defect sites in $FeTiO_3$/C. This is consistent with its XRD pattern shown in Fig. 1b, where no diffraction peak due to the crystalline phase of carbon was observed. The presence of amorphous carbon with rich defect sites and good electrical conductivity in $FeTiO_3$/C can modulate and tune the electronic structure of $FeTiO_3$ for enhanced adsorption and catalytic performances[39,43].

$FeTiO_3$/C exhibited a type IV N_2 adsorption-desorption isotherm with an H3-type hysteresis loop in the relative pressure (P/P_0) range from 0.6 to 1.0 due to capillary condensation inside the secondary inter-particle mesopores (Fig. 4c). $FeTiO_3$/C had a larger specific surface area (S_{BET}: 159.0 m^2 g^{-1}) than natural ilmenite (1.7-6 m^2 g^{-1}[12,13,20]) and other synthetic $FeTiO_3$ nanoparticles (e.g., 58.4 m^2 g^{-1} for $FeTiO_3$ hollow spheres[44], 139.5 m^2 g^{-1} for $FeTiO_3$ nanohexagons[45]). The average pore diameter D_p in $FeTiO_3$/C was estimated to be 8.8 nm by $D_p = 4000V_P/S_{BET}$, where the pore volume V_p is 0.35 cm^3 g^{-1}. The larger S_{BET} and D_p values of $FeTiO_3$/C are beneficial for rapid mass transport of reactants to access large amounts of surface active sites for enhanced adsorption and catalysis.

The pH_{pzc} of $FeTiO_3$/C was determined to be 3.30 (Fig. 4d). It renders the surface of $FeTiO_3$/C particles nearly neutral or slightly positive charge at the typical pH value (~3) used in Fenton oxidation, which is critical for wide applications of $FeTiO_3$/C in the degradation of organic pollutants with different charges via CWPO.

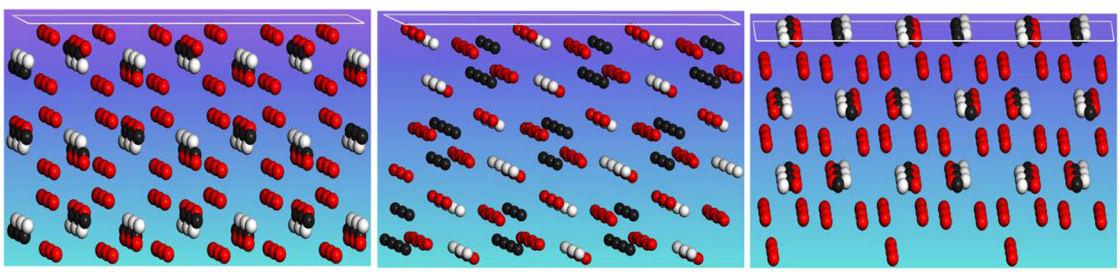

Fig. 2 Side views of (3 × 3) supercells built by cleaving the $FeTiO_3$ lattice along different crystal planes with fractional thickness of 3.0. **a** (104), **b** (012), and **c** (110). The numbers in Å indicate lattice parameters. Atomic representation: black—Fe, white—Ti, and red—O.

The SEM image of $FeTiO_3$/C (Fig. 5a) displayed aggregated nanoparticles with inter-particle pores, which account for the appearance of a hysteresis loop at high P/P_0 in the N_2 adsorption-desorption isotherm (Fig. 4c). Its TEM image (Fig. 5b) mainly contains elongated or ellipsoidal nanoparticles (length: 63.0±15.4 nm and diameter: 24.0±10.2 nm in Supplementary Fig. 1), which were also supported by the HRTEM image taken on thin areas of the TEM specimen (Fig. 5c). The clear lattice image across a whole particle in region I of Fig. 5c was observed in Fig. 5d, indicative of its single-crystalline structure. The lattice fringe of a big particle in region II of Fig. 5c was displayed in Fig. 5e. The interlayer spacing was measured by Digital Micrograph to be 0.374 nm in region I (Fig. 5f) and 0.254 nm in region II (Fig. 5g), which well match with those of the (012) and (110) planes of the $FeTiO_3$ lattice. This is in agreement with the XRD results and supports the preferential growth of (012) and (110) planes in $FeTiO_3$/C-0.67. In addition, amorphous carbons were also observed along the boundaries of $FeTiO_3$ crystal lattices in HRTEM. The interfaces between them were delineated with red curves in Fig. 5d and e, indicating the formation of closely contacted $FeTiO_3$/C nanocomposite.

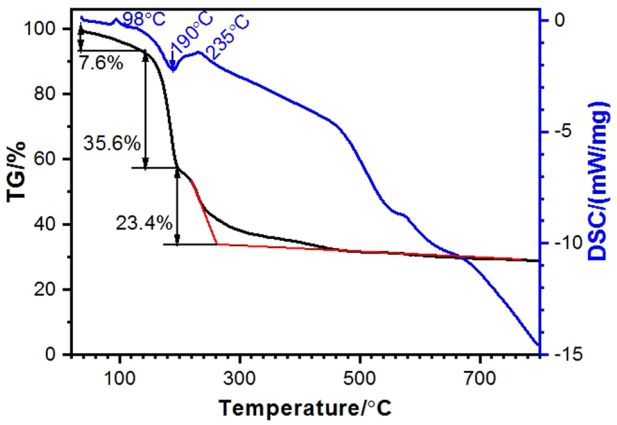

Fig. 3 TG-DSC curves of CTAB-containing gel precursor in N_2.

The elemental composition and chemical states on the surface of $FeTiO_3$/C were characterized by XPS. The XPS survey spectrum in Fig. 6a confirmed the presence of Fe, Ti, O, C and N elements on the surface with the atomic ratio of 2.1Fe : 1.0Ti : 3.3 O : 8.5 C : 0.50 N. The asymmetrical C 1 s peak (Fig. 6b) were deconvoluted into three peaks at 284.5, 285.8 and 288.9 eV, which could be assigned to the C–C, C–N and C–O bonds, respectively[46]. Two weak peaks at 398.2 and 400.5 eV in the N 1 s spectrum (Fig. 6c) indicated that a small amount of nitrogen exists in two different chemical states, which may be respectively derived from the decomposition of CTAB and TEA. The O 1 s XPS spectrum (Fig. 6d) could be fitted into two peaks at 528.6 and 530.0 eV, respectively. The former was assigned to lattice oxygen (O_L) in $FeTiO_3$, and the latter may be attributed to defect oxygen components such as chemisorbed hydroxyl groups or oxygen vacancies (O_V) in $FeTiO_3$/C[45,47]. The EPR technique is usually used to detect O_V with the appearance of a typical paramagnetic signal at $g = 2.001$[47]. However, the EPR spectrum of $FeTiO_3$/C (Supplementary Fig. 2) cannot convincingly support the presence of O_V because of strong interference from a large amount of iron present in $FeTiO_3$/C, which can mask the O_V signal by the generation of substantially overlapped EPR signals at similar positions[48,49]. The surface Fe/Ti ratio of 2.1 was obviously larger than the nominal Fe/Ti ratio of 1.0 or EDX-analyzed Fe/Ti ratio of 0.8 (Fig. 4a), indicating iron enrichment on the surface of $FeTiO_3$/C. The Ti 2p XPS spectrum in Fig. 6e contained two main peaks at about 462.6 (Ti $2p_{1/2}$) and 456.9 eV (Ti $2p_{3/2}$) due to spin-orbit splitting. The Ti 2p line shapes are asymmetric with the peak tailing to the higher binding energy. The Ti $2p_{3/2}$ peak at ~456.9 eV is located between Ti^0 (454.1 eV) and Ti^{4+} (458.8 eV), and could be deconvoluted into two components at 457.7 and 456.9 eV. Similarly, the Ti $2p_{1/2}$ peak was fitted into two peaks at 463.8 and 462.4 eV (Fig. 6e). It indicates that Ti exists in mixed oxidation states in $FeTiO_3$/C but Ti^{3+} is dominant with binding energies at 456.9 eV (Ti^{3+} $2p_{3/2}$) and 462.4 eV (Ti^{3+} $2p_{1/2}$)[45]. In accordance with the Ti 2p spectrum, the Fe 2p spectrum was also deconvoluted into two components

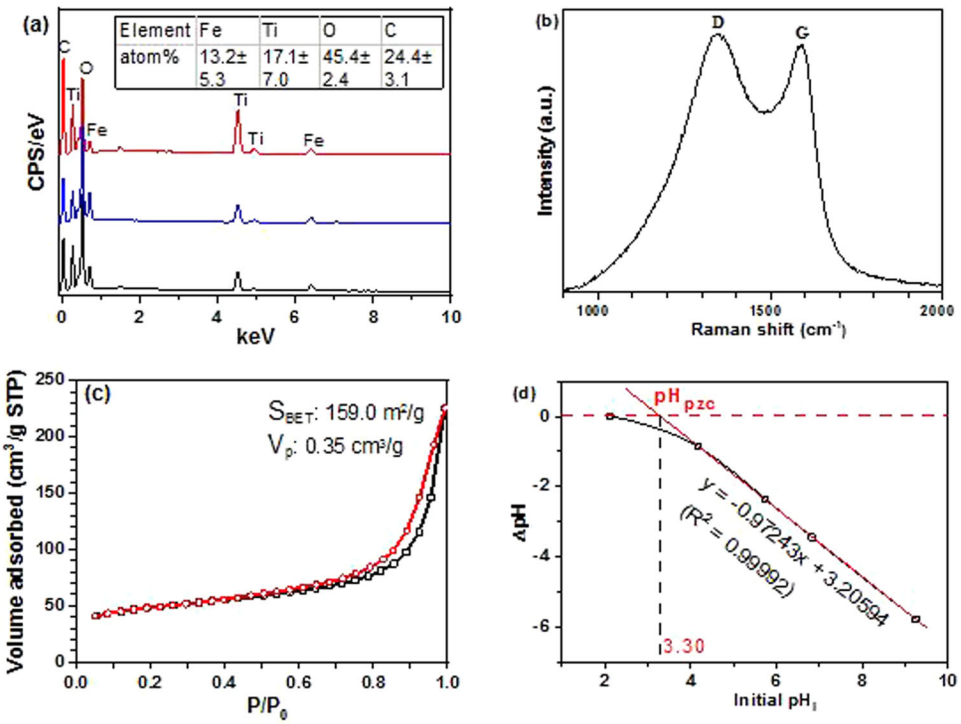

Fig. 4 Characterizations of $FeTiO_3$/C. a EDX spectra, **b** Raman spectrum, **c** N_2 adsorption-desorption isotherm, and **d** Measurement of pH_{pzc}.

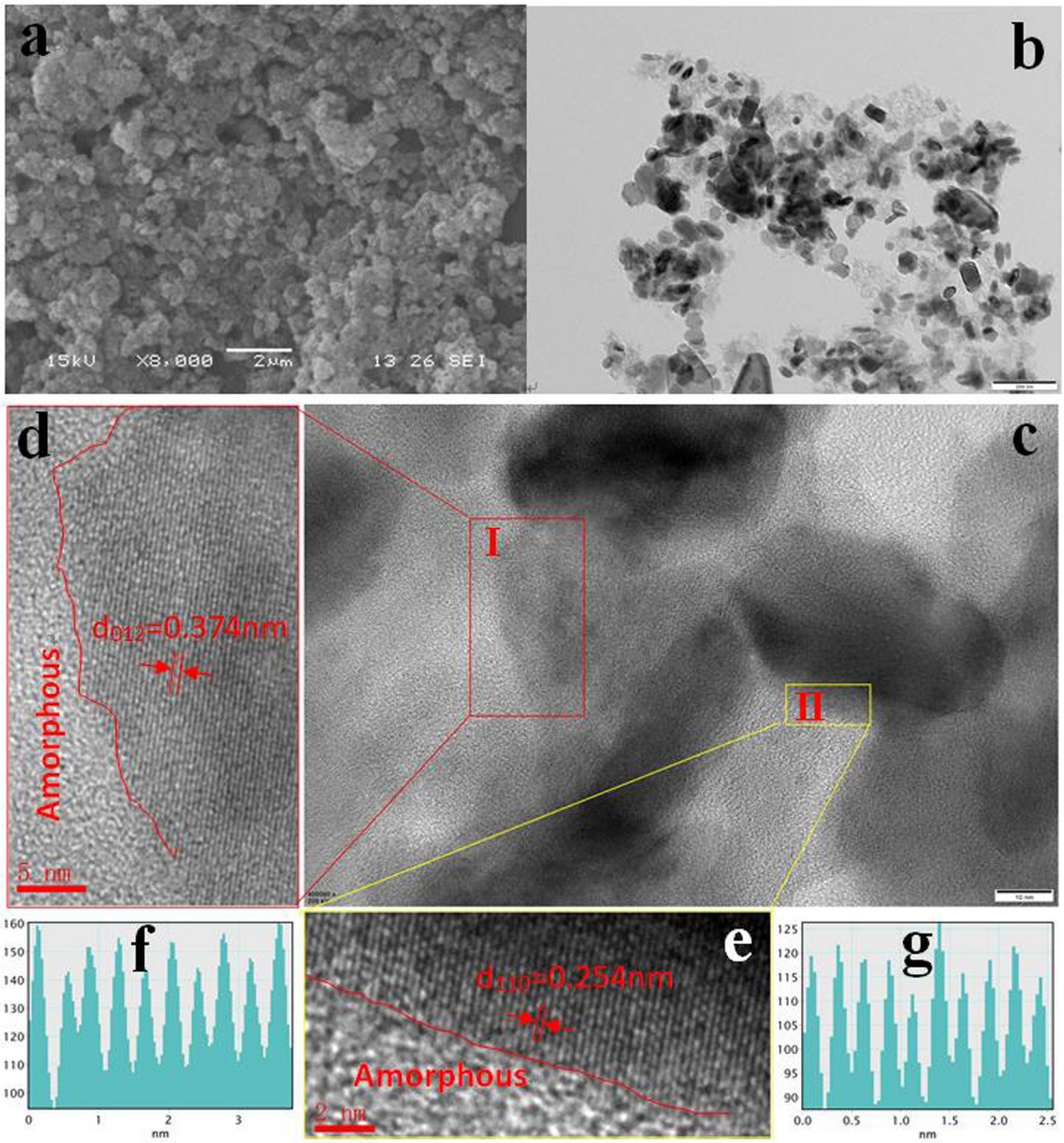

Fig. 5 Electron microscope images of $FeTiO_3$/C. a SEM, **b** TEM, and **c**–**e** HRTEM. The d-spacing values in images (**d**, **e**) were respectively measured from line profiles (**f**, **g**). The scale bars in (**a**–**e**) represent 2 μm, 200 nm, 10 nm, 5 nm and 2 nm, respectively.

(Fig. 6f), which were respectively assigned to Fe^{2+} (722.9 and 709.1 eV) and Fe^{3+} (724.5 and 710.9 eV) with the Fe^{2+}/Fe^{3+} ratio of about 2.0[50]. According to the surface elemental composition and surface Fe^{2+}/Fe^{3+} ratio obtained from XPS analysis, the atomic percentage of surface Fe^{2+} and Fe^{3+} on $FeTiO_3$/C was estimated to be about 9.1% and 4.5%, respectively. In comparison, the surface Fe^{2+}/Fe^{3+} ratio of $FeTiO_3$ synthesized without the addition of CTAB was only about 0.34 (Supplementary Fig. 3), which supports that the introduction of CTAB leads to a significant enrichment of Fe^{2+} species on the surface of $FeTiO_3$/C. The presence of multiple oxidation states of iron and titanium in $FeTiO_3$ has been reported in the literature[24,45]. It is worthy to note that their low-valent oxidation states (Fe^{2+} and Ti^{3+}) are predominant on the $FeTiO_3$/C surface, which was attributed to in-situ carbothermal reduction[37] of $FeTiO_3$ during pyrolysis of CTAB-containing gel precursor at 700 °C in N_2. In addition, the reduction of Fe^{3+} by Ti^{3+} (Eq. 2) is thermodynamically favorable according to standard potentials of Fe^{3+}/Fe^{2+} (0.771 V) and TiO^{2+}/Ti^{3+} (0.10 V), which further increases the amount of Fe^{2+} on the $FeTiO_3$/C surface. It is expected that the presence of multiple oxidation states, surface-enriched Fe^{2+} ions and abundant defective sites change the surface electronic states and properties of $FeTiO_3$/C for its enhanced catalytic activity[45].

$$Fe^{3+} + Ti^{3+} + H_2O = Fe^{2+} + TiO^{2+} + 2H^+ \ (\Delta E^o = 0.671V) \quad (2)$$

CWPO removal of aromatic pollutants on $FeTiO_3$/C nanocomposites

Widely used aromatic compounds have been considered as priority pollutants because of harmful effects on the ecosystem and human health due to their refractory and bio-accumulative nature. In this work, six model pollutants in Table 1 have been selected to represent aromatic compounds with different charges, including cationic RhB and MB dyes, anionic OG dye and three neutral pharmaceuticals, for evaluation of the catalytic performance of $FeTiO_3$/C as a heterogeneous Fenton-like catalyst. TC

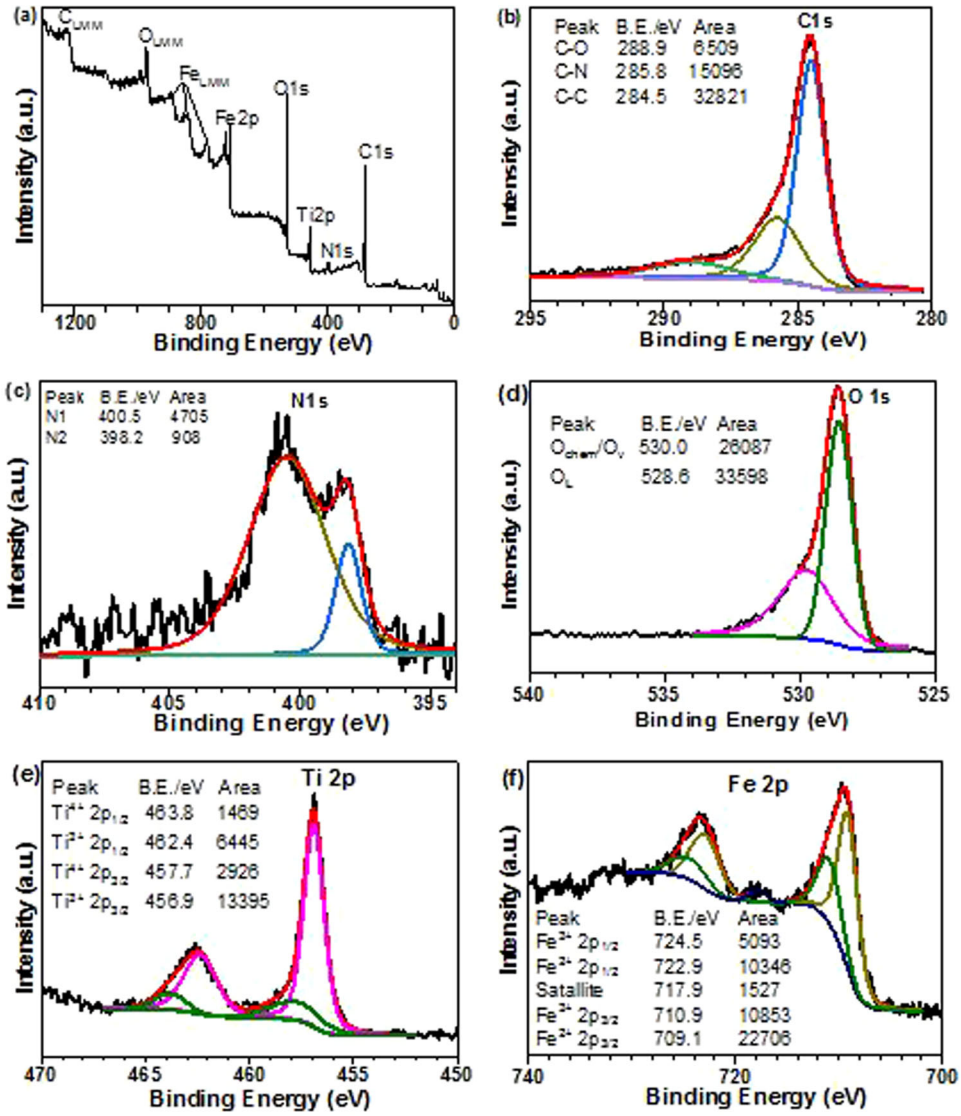

Fig. 6 XPS spectra of $FeTiO_3$/C nanoparticles. a Survey spectrum, **b** C1s, **c** N1s, **d** O 1s, **e** Ti 2p, and **f** Fe 2p.

was chosen as the initial compound to compare the catalytic activities of various $FeTiO_3$/C samples made under different conditions because of its slow degradation rate. As seen in Fig. 7a, $FeTiO_3$/C-0.67 performed the best for TC degradation, followed in order by $FeTiO_3$/C-1.33, $FeTiO_3$/C-0 and $FeTiO_3$/C-NT. In agreement with the XRD results in Fig. 1a, slightly lower activity of $FeTiO_3$/C-1.33 could be due to the presence of minor rutile phase with low activity for H_2O_2 activation, and low activity of $FeTiO_3$/C-NT may be related to its low crystallinity due to no addition of TEA during its preparation. The lowest activity of $FeTiO_3$/C-0, which was prepared without the addition of CTAB, reflected the importance of CTAB-derived carbon component in $FeTiO_3$/C-0.67 for its improved activity.

The wide applicability of $FeTiO_3$/C-0.67 was then tested for degradation of the other model pollutants in Table 1. As shown in Fig. 7b, all tested pollutants were effectively degraded over $FeTiO_3$/C-0.67 with 93–100% of DRs after reacting with H_2O_2 for 3 h at pH 3.0 and 25 °C. It is noteworthy that $FeTiO_3$/C-0.67 with pH_{zpc} of 3.3 (Fig. 4d) can effectively catalyze the degradation of differently charged organic pollutants with H_2O_2 at pH 3.0, which is attributable to the weak electrostatic repulsion between organic molecules and its nearly neutral surface. This was also supported by the low zeta potential of $FeTiO_3$/C-0.67, which was measured to be 5.95 ± 0.51 mV (Supplementary Fig. 4) at pH 3.0 and 25 °C. In this case, non-electrostatic interactions such as hydrogen bond, π-π interaction with graphitic carbon (Fig. 4b) or cation-π interaction with metallic sites on $FeTiO_3$/C[51–53], may become the main driving forces for the adsorption of π-conjugated aromatic compounds on $FeTiO_3$/C for subsequent degradation with H_2O_2. As a simplified example, the inter-molecular interaction between neutral APAP molecule and graphitic carbons was estimated to about 9.1 kJ mol^{-1} by DFT calculation (Supplementary Fig. 5 and Supplementary Table 1).

In comparison with the degradation of antibiotics, decolorization of dye solutions was more efficient in the H_2O_2-$FeTiO_3$/C system—after reacting for 1 h at pH 3.0 and 25 °C, three dye solutions (MB, RhB or OG) were completely decolorized while the DRs of three antibiotics were 56.6% for MNZ, 76.1% for TC and 91.2% for APAP. The degradation processes of the six tested pollutants were well fitted with pseudo-first-order kinetic model (Supplementary Fig. 7) with the rate constant k_{s1} varying between 0.0101 min^{-1} for TC and 0.0802 min^{-1} for OG ((Fig. 7b inset). No induction period was observed on $FeTiO_3$/C-0.67 due to its larger surface Fe^{2+}/Fe^{3+} ratio of 2.0. In comparison, when Fe^{3+} is the prevailing form in other iron-based catalysts such as ferrihydrite and FeOCl[54,55], Fenton-active Fe^{2+} has to be first generated by

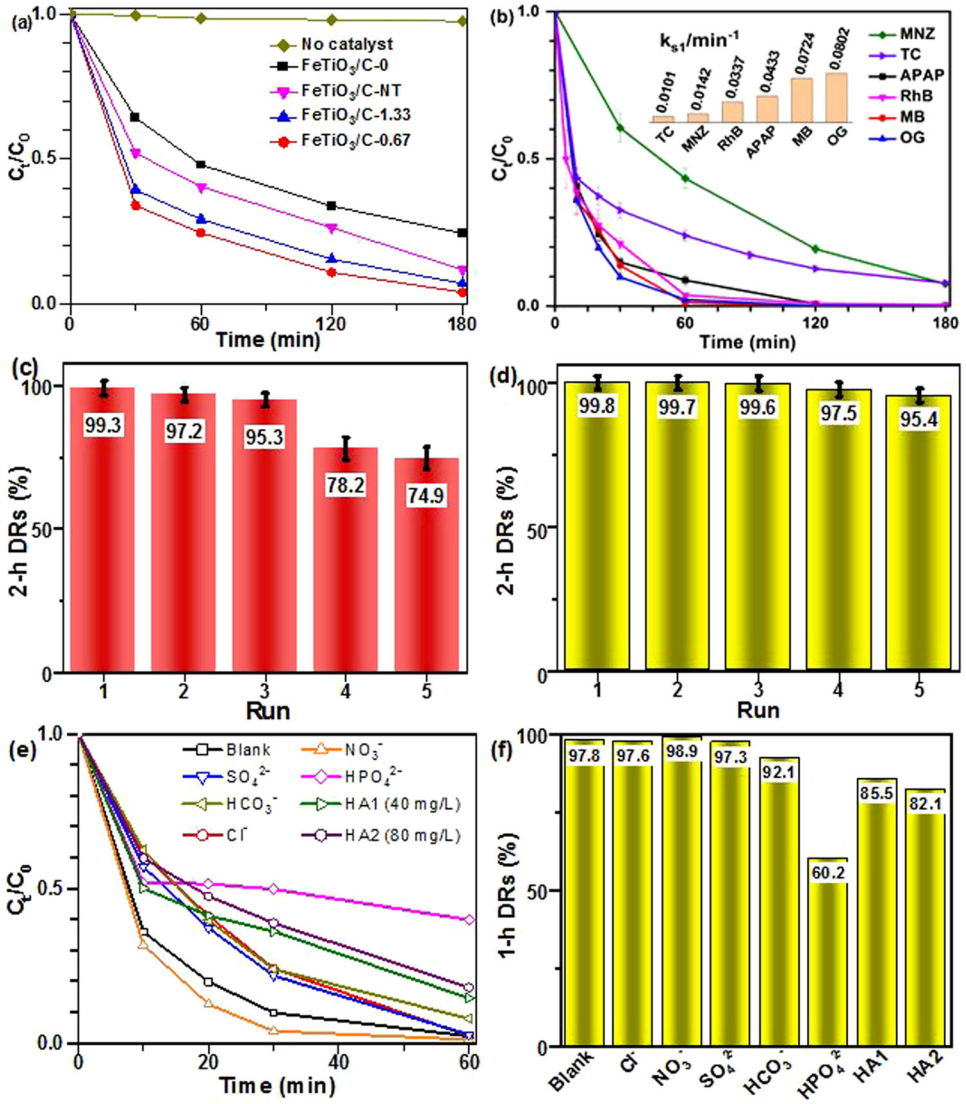

Fig. 7 Catalytic performances of $FeTiO_3$/C. a C_t/C_0 – time plots for TC degradation on different samples. **b** C_t/C_0 – time plots for degradation of different pollutants on $FeTiO_3$/C-0.67. **c**, **d** Recyclability of $FeTiO_3$/C-0.67 for decolorization of the solutions of RhB (**c**) and OG (**d**). **e**, **f** Effects of different anions (10 mM each) and humic acid (40 or 80 mg/L added) on decolorization of the OG solution. Unless otherwise specified, reaction conditions were 25 mg/L pollutants, 40 mM H_2O_2, 0.5 g/L catalysts, pH 3.0 and 25 °C. Error bars in (**b**–**d**) were defined as standard deviation.

slow reduction of Fe^{3+} with H_2O_2 (Eq. 3) in order to increase the generation rate of •OH. For example, a 3 h induction period was experienced when natural ilmenite mineral with surface Fe^{2+}/Fe^{3+} ratio of 0.56 was exploited as a CWPO catalyst for phenol degradation at pH 3 and 25 °C[12].

$$\equiv Fe^{3+} + H_2O_2 \rightarrow \equiv Fe^{2+} + H^+ + HOO\bullet (\equiv \text{represents particle surface}) \quad (3)$$

Natural ilmenite had negligible activity in degrading phenol with H_2O_2 at pH 3.0 and 75 °C in the second and third runs due to strong deactivation[3]. In this work, good reusability of $FeTiO_3$/C-0.67 was testified by decolorization of RhB or OG solution (25 mg L^{-1} each) with H_2O_2 (40 mM) at pH 3.0 and 25 °C. The 2 h DRs of RhB solution were 99.3%, 97.2%, 95.3%, 78.2% and 74.9% in five consecutive runs (Fig. 7c) with the COD reduction of about 83.0%. The 2 h DRs of OG solution in five cycles were 99.8%, 99.7%, 99.6%, 97.5% and 95.4% (Fig. 7d) with the COD reduction of about 74.5%. It is noteworthy that $FeTiO_3$ particles synthesized without adding CTAB ($FeTiO_3$/C-0 in Fig. 1c) gradually lost the catalytic activity in recyclability tests (e.g., 2 h DRs of OG solution were 99.7%, 98.6%, 92.7%, 72.4% and 39.1% in five consecutive runs, Supplementary Fig. 6), which indicates that carbon in $FeTiO_3$/C contributes to its improved activity and stability by the formation of close contact between $FeTiO_3$ and carbon as seen in Fig. 5d and e by HRTEM.

The $FeTiO_3$/C catalyst after recyclability tests was recovered for further characterization by XRD, SEM, Raman spectroscopy and XPS (Supplementary Fig. 8). Some additional diffraction peaks besides those of ilmenite appeared in the XRD pattern of the recovered $FeTiO_3$/C (Supplementary Fig. 8a), which indicated the formation of TiO_2 (rutile) impurity due to slow acid leaching of iron after $FeTiO_3$/C has been used five times at pH 3. Other than the rutile impurity, the recovered $FeTiO_3$/C displayed the Raman spectrum and SEM image (Supplementary Fig. 8(b,c)) similar to the fresh catalyst, which supports the stabilizing role of carbon component in $FeTiO_3$/C. According to the XPS survey spectrum (Supplementary Fig. 8d), the recycled $FeTiO_3$/C catalyst contained the same surface elements (Fe, Ti, O, C and N) as the fresh one, but had different atomic ratios (fresh: 2.1Fe : 1.0Ti : 3.3 O : 8.5 C : 0.50 N

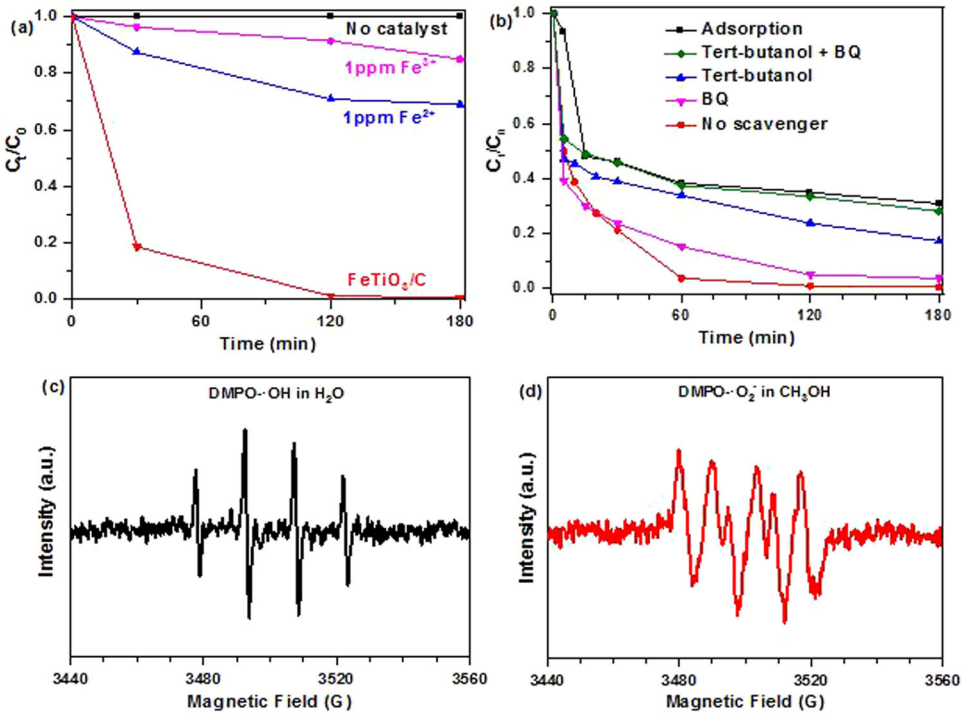

Fig. 8 Mechanistic studies. a Degradation of RhB in homogeneous Fe^{2+} or Fe^{3+} system. **b** Scavenging tests during RhB degradation on $FeTiO_3$/C. EPR spectra of **c** DMPO-•OH in H_2O and **d** DMPO-$O_2^{\bullet-}$ in methanol in the presence of H_2O_2 and $FeTiO_3$/C.

vs. recycled: 1.4Fe : 1.0Ti : 8.0 O : 23.1 C : 0.46 N). Higher contents of carbon and oxygen at the surface of the recycled catalyst were attributable to the adsorption of degradation intermediates and water, which were supported by the enhanced C-O signal at 288.7 eV in its C 1 s XPS spectrum (Supplementary Fig. 8e) and a new peak at 533.0 eV due to adsorbed water in its O 1 s XPS spectrum (Supplementary Fig. 8f). The N 1 s XPS spectrum of the recycled catalyst (Supplementary Fig. 8g) had only one peak at 399.7 eV, indicating that the minor N species at 398.2 eV in the fresh catalyst was unstable during the degradation of OG with H_2O_2. Similar to the fresh one, the Ti 2p and Fe 2p XPS spectra of the recycled catalyst consisted of two sets of doublets (Supplementary Fig. 8(h,i)), indicating the mixed valence states of Ti and Fe. The surface Fe^{2+}/Fe^{3+} ratio of the recycled catalyst was estimated to be 0.6 from its Fe 2p XPS spectrum (Supplementary Fig. 8i), which is slightly higher that of $FeTiO_3$ (0.5) synthesized without the addition of CTAB, but lower than that of the fresh $FeTiO_3$/C (2.0) due to slow regeneration of Fe^{2+} ions during Fe^{3+}/Fe^{2+} redox cycling. The decrease in surface Fe^{2+} content and adsorption of degradation intermediates gradually reduced the catalytic activity of the recycled catalyst.

A series of tests were carried out to investigate the effects of different anions (NO_3^-, Cl^-, SO_4^{2-}, HCO_3^- or HPO_4^{2-}) and varying natural water conditions on the catalytic performance of $FeTiO_3$/C (Fig. 7(e,f)). Three types of anionic effects could be found in Fig. 7e. Firstly, the addition of NO_3^- enhanced the OG decolorization efficiency - the k_{s1} increased from 0.0802 min^{-1} in blank experiment to 0.108 min^{-1} with the addition of 10 mM of NO_3^-. This may be attributed to higher ionic strength in the NO_3^--containing solution, which enhanced the adsorption and decolorization of OG on $FeTiO_3$/C. Secondly, the addition of SO_4^{2-}, Cl^- and HCO_3^- (10 mM each) moderately inhibited the OG decolorization - k_{s1} decreased from 0.0802 min^{-1} in blank experiment to 0.051, 0.047 and 0.047 min^{-1}, respectively, with the addition of SO_4^{2-}, Cl^- and HCO_3^-. This may be related to radical-scavenging effects of these anions[56–58]. In spite of different reaction rate constants, the 1 h DRs of OG (92.1%–98.9% in Fig. 7f) were not obviously affected by the addition of NO_3^-, Cl^-, SO_4^{2-} or HCO_3^- in the H_2O_2 - $FeTiO_3$/C system. Thirdly, the presence of 10 mM of HPO_4^{2-} significantly slowed down the OG decolorization (1 h DRs decreased from 97.8 to 60.2%) and the decolorization process of OG could not be well fitted by pseudo-first-order reaction model possibly due to strong interference from competitive adsorption of PO_4^{3-} on $FeTiO_3$/C. To check the effect of natural organic matter, humic acid (HA, 40 or 80 mg L^{-1}) was also intentionally added during the OG decolorization in the H_2O_2-$FeTiO_3$/C system. HA had some negative impact on the OG decolorization (1 h DR decreased to 82.1% in the presence of 40 mg L^{-1} of HA). However, 1 h DR still kept at 82.1% even at 80 mg L^{-1} of HA, which supports potential applicability of $FeTiO_3$/C at varying water conditions.

Mechanistic studies

The concentration of the total soluble iron leached into solution during the degradation of RhB over $FeTiO_3$/C-0.67 was 0.57 mg L^{-1}. When 1.0 ppm of Fe^{2+} or Fe^{3+} ($FeSO_4{\cdot}7H_2O$ or hydrated $Fe_2(SO_4)_3$ used as soluble iron source, respectively) was added to replace $FeTiO_3$/C as homogeneous catalysts under otherwise identical conditions, the 2 h DR of RhB (25 mg L^{-1}) was only 29.2% or 15.1% (Fig. 8a). These control experiments and the above-described recyclability tests supported that the RhB degradation with H_2O_2 was mainly a heterogeneous catalytic process occurring on the surface of $FeTiO_3$/C-0.67.

The reactive oxygen species (ROS) involved in the H_2O_2-$FeTiO_3$/C system was investigated by scavenging experiments during the RhB degradation. Tert-butanol (TBA) and p-benzoquinone (BQ) were used to scavenge ·OH and $O_2^{\bullet-}$ radicals, respectively[59–61]. As can be seen in Fig. 8b, the 2 h DR of RhB (25 mg L^{-1}) decreased from 99.5% to 76.0% upon the addition of 50 mM of TBA, which is about 1000 times the RhB concentration (0.052 mM). In contrast, it only slightly dropped to 96.5% in the presence of 5 mM of BQ. Higher concentration of BQ has not been tested because of its low solubility in water. It is important to note that the decolorization process of RhB solution with the co-addition of H_2O_2, TBA and BQ was very similar to the adsorption of RhB on $FeTiO_3$/C. It implied

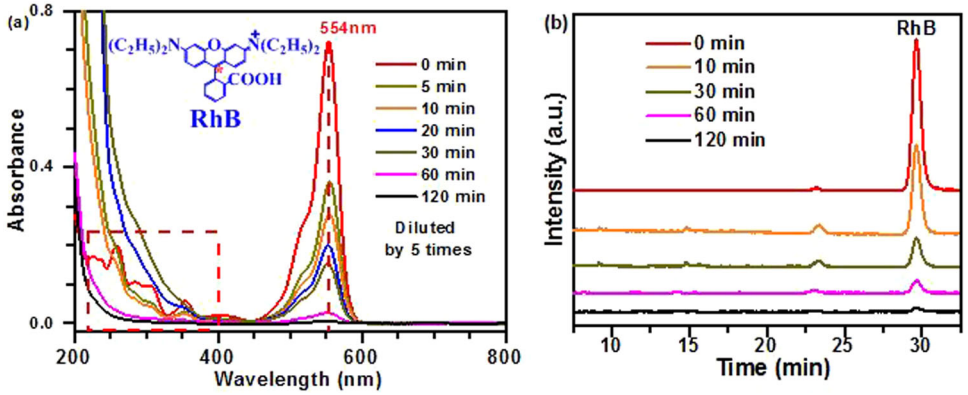

Fig. 9 Monitoring catalytic degradation of RhB with H_2O_2 over $FeTiO_3$/C. a UV-Vis spectra and **b** HPLC chromatograms. Experimental conditions: RhB (25 mg/L), catalyst (0.5 g/L) and H_2O_2 (40 mM) at pH 3 and 25 °C.

that the addition of both TBA and BQ almost completely inhibited the degradation of RhB. The scavenging experiments indicated that ·OH radicals are the main ROS while $O_2^{\bullet-}$ make a minor contribution to the degradation of RhB with H_2O_2 over $FeTiO_3$/C.

EPR spectra were also recorded with DMPO as a spin-trapping agent to identify the generation of ·OH and $O_2^{\bullet-}$ radicals. A typical 1:2:2:1 quadruplet pattern corresponding to the DMPO-·OH adduct was observed in Fig. 8c, confirming the formation of ·OH radicals upon mixing H_2O_2 with $FeTiO_3$/C in water. The DMPO-$O_2^{\bullet-}$ signals were also detected in methanol in Fig. 8d. Both scavenging tests and EPR spectra supported the formation of dominant ·OH and minor $O_2^{\bullet-}$ upon catalytic decomposition of H_2O_2 on $FeTiO_3$/C.

The ·OH radicals can be generated from reductive decomposition of H_2O_2 on low-valent metallic sites (Fe^{2+} or Ti^{3+}) on the surface of $FeTiO_3$/C (Eq. 4). The high-valent metallic sites are again reduced to low-valent states by H_2O_2 to complete the catalytic cycles, during which the HOO•/$O_2^{\bullet-}$ radicals were formed in the system (Eq. 5). The ·OH and $O_2^{\bullet-}$ radicals as reactive intermediates then attack and degrade electron-rich π-conjugated aromatic molecules (e.g., RhB) adsorbed on the surface of $FeTiO_3$/C.

$$\equiv M^{n+1+} + H_2O_2 \rightarrow \equiv M^{(n+1)+} + \bullet OH + OH^- (\text{M for Fe or Ti}) \quad (4)$$

$$\equiv M^{(n+1)+} + H_2O_2 \rightarrow \equiv M^{n+} + H^+ + HOO\bullet \quad (5)$$

As shown in Fig. 9a, during the RhB degradation over $FeTiO_3$/C, the peak intensity of its characteristic absorption (λ_{max}) at 554 nm gradually decreased and several small absorption bands before 400 nm quickly diminished before 5 min. The degradation of RhB molecules (Fig. 9a inset) generally proceeds via two different pathways: N-de-ethylation or chromophore cleavage, followed by hydroxylation, ring opening or mineralization[14,62,63]. N-de-ethylation causes a hypsochromic shift in λ_{max} of the residual solution because of the auxochromic property of N-ethyl groups[14,62,63], while chromophore cleavage only reduces the absorbance at 554 nm. No shift in λ_{max} was observed during the entire course of the RhB degradation in the H_2O_2-$FeTiO_3$/C system (Fig. 9a), implying that the RhB degradation mainly proceeds via the chromophore cleavage under our experimental conditions. It was supported by the HPLC histograms of degradation solution at different times (Fig. 9b), in which very weak or negligible peaks due to N-de-ethylation intermediates were observed.

CTAB played critical roles in making highly active and stable $FeTiO_3$/C catalyst. Firstly, it facilitated the growth of the (110) and (012) crystal planes with more metallic sites exposed on the surface upon selective adsorption on the (104) plane. Secondly, CTAB-derived carbon components restricted the growth of $FeTiO_3$ nanoparticles and partially reduced Fe^{3+} to Fe^{2+} during pyrolysis due to close contact between $FeTiO_3$ and C, thus generating $FeTiO_3$/C composite with high surface area and rich ferrous content. Thirdly, the adsorption of aromatic pollutants via π-π interaction and electron transfer process during CWPO may be enhanced by graphitic and disordered carbons present in $FeTiO_3$/C.

In conclusion, anisotropic ilmenite/carbon ($FeTiO_3$/C) nanocomposite with abundant interfacial ferrous ions was synthesized via CTAB-assisted sol-gel method in this work. $FeTiO_3$/C exhibited high activity and good recyclability as a heterogeneous Fenton-like catalyst for CWPO removal of differently charged aromatic pollutants. Scavenging tests and spin-trapping EPR spectra confirmed that •OH and •O_2^- are the primary reactive species for pollutant degradation in H_2O_2 - $FeTiO_3$/C catalytic system.

METHODS

Chemicals and regents

$Fe(NO_3)_3{\cdot}9H_2O$, tetrabutyl titanate (TBOT), triethylamine (TEA), CTAB, rhodamine B (RhB), methylene blue (MB), orange G (OG), tetracycline hydrochloride (TC), metronidazole (MNZ), acetaminophen (APAP), p-benzoquinone (BQ), tert-butanol, H_2O_2 (30%), NaCl, KNO_3, Na_2SO_4, $NaHCO_3$ and $Na_2HPO_4{\cdot}12H_2O$ were purchased from Sinopharm Chemical Reagent (Shanghai, China). Humic acid was obtained from Yuanye Biotechnology (Shanghai, China). 5,5-Dimethyl-1-pyrrolidine N-oxide (DMPO) was supplied by Sigma-Aldrich (Shanghai, China). All chemicals were of analytic grade or above and used as received. All aqueous solutions were prepared with deionized (DI) water (<20 μS cm^{-1}) produced from Heal Force NW 15VF.

CTAB-assisted sol-gel synthesis of $FeTiO_3$/C

In a typical synthesis, 1.4540 g (3.6 mmol) of $Fe(NO_3)_3{\cdot}9H_2O$ was dissolved in 10 mL of ethanol, followed by addition of 1.2290 g (3.6 mmol) of TBOT, 10 mL of CTAB solution in ethanol and 2 mL (14.4 mmol) of TEA to get a reaction mixture with molar composition of 1.0Fe : 1.0Ti : xCTAB : 4.0TEA (x = 0, 0.67 or 1.33). Note that the $FeTiO_3$/C used in this work was generally synthesized with x = 0.67 if not specified. The whole mixture was heated at 70 °C to form a brown gel precursor, which was then converted to $FeTiO_3$/C by heating in N_2 at 700 °C for 2 h in a tube furnace with a heating rate of 5 °C min^{-1} from 25 °C to 700 °C.

Characterization of $FeTiO_3$/C nanocomposites

Powder X-ray diffraction (XRD) patterns were collected on Bruker D8 Advance Diffractometer with Cu Kα radiation at 30 kV and 20 mA. Surface cleavage of the $FeTiO_3$ lattice was performed on Materials Studio 7.0. Thermogravimetric-differential scanning calorimetry (TG-DSC) analysis was carried out in N_2 on Netzsch STA 449F3 from room temperature to 800 °C at a heating rate of

10 °C min^{-1}. Raman spectrum was recorded on Thermo Scientific DXR with a 532 nm excitation laser source. N_2 physisorption analysis was measured on Micromeritics ASAP 2020 at 77 K. The sample was degassed at 150 °C for 4 h under vacuum before measurement. The BET specific surface area S_{BET} was calculated from the adsorbed amount of N_2 in the relative pressure (P/P_0) range of 0.05–0.30. The pore volume V_p was converted from the adsorbed quantity of N_2 at $P/P_0 = 0.99$. The point of zero charge (pH_{pzc}) was determined by the conventional method[64,65]. In brief, 0.20 g of $FeTiO_3$/C was dispersed into 20 mL of 0.10 M NaCl after adjusting its initial pH (pH_i) to 2–10 via HCl or NaOH solutions. After the suspensions were agitated in a shaker at 150 rpm and 30 °C for 8 h, the final pH values (pH_f) were recorded. The pHzpc was determined by the intersection point of the ΔpH - pH_i plot at $\Delta pH = 0$, where $\Delta pH = pH_f - pH_i$. Zeta potentials were measured on Malvern Zetasizer Pro. Scanning electron microscope (SEM) images were taken on JEOL JSM-5510LV SEM at 20 kV. Energy-dispersive X-ray spectroscopy (EDX, Oxford Instruments) attached to SEM was used for elemental analysis. Transmission electron microscope (TEM) and high-resolution TEM (HRTEM) images were taken on JEM-2100 TEM at 200 kV. The particle size and interlayer spacing were respectively measured by ImageJ and Digital Micrograph. X-ray photoelectron spectroscopy (XPS) analyses were conducted on X-ray Photoelectron Spectrometer (ESCALAB 250XI XPS Thermo Company, America) using a monochrome Al Kα radiation ($h\nu = 1486.6$ eV) as the excitation source. The C 1 s peak of adventitious carbon at 284.8 eV was used as charge reference.

CWPO of aromatic pollutants over $FeTiO_3$/C nanocomposites

Six aromatic compounds in Table 1 were employed to evaluate the performance of $FeTiO_3$/C in CWPO. Typically, 0.025 g of $FeTiO_3$/C was added into 50 mL of aqueous solution of an organic pollutant (25 mg L^{-1}, pH adjusted to ~3 by 1 M H_2SO_4) at 25 ± 2 °C and 750 rpm. The degradation was initiated by adding 0.230 g of H_2O_2 (30%) into the solution. About 3 mL of aliquots were sampled at given intervals by syringe and passed through a 0.22 µm filter membrane before analyzing the concentration of residual pollutants. In recyclability tests, the used $FeTiO_3$/C was recovered by centrifugation after each run for 3 h, and directly re-used according to the same degradation procedure.

The degradation or decolorization rate (in short DR) of organic pollutants was defined as $DR = (1 - C_t/C_0) \times 100\%$, where C_0 and C_t were the respective concentrations of organic pollutants at time zero and elapsed time (min). The concentrations of RhB, MB, OG, TC and MNZ in water were analyzed by measuring the absorbance at 554, 664, 478, 357 and 320 nm, respectively, using a UV-Vis spectrophotometer (UV-1800PC, Shanghai Mapada Instrument) (Supplementary Fig. 9(a–e)). High concentrations of RhB and MB solutions were diluted by five times before measurement. The APAP concentration in water was measured by high-performance liquid chromatography (HPLC, Shimadzu LC-2050C 3D with a DAD detector or Thermo Fisher Ultimate 3000 with a UV-Vis detector) equipped with an Analytical C18 column (150 mm × 4.6 mm, packed with 5 µm particles) at 35 °C (Supplementary Fig. 9f). The mobile phase was the mixture of methanol and water (55:45 by volume) with a flow rate of 0.8 mL min^{-1} and UV-Vis detector was set at 248 nm. The total soluble iron content leached into solution from $FeTiO_3$/C after the reaction was analyzed by 1,10-phenanthroline spectrophotometric method with hydroxylamine hydrochloride as a reducing agent. The chemical oxygen demand (COD) was determined according to China National Standard GB11892-89 (ISO8467-1993).

Determination of reactive oxygen species

Reactive oxygen species (ROS) were determined by scavenging experiments and electron paramagnetic resonance (EPR) measurements. In scavenging tests, a suitable quencher (tert-butanol for •OH and BQ for $O_2^{\bullet-}$) was added during the degradation of RhB with H_2O_2 over $FeTiO_3$/C. During EPR measurements, DMPO was added as a spin-trapping agent for •OH in H_2O or for $O_2^{\bullet-}$ in methanol. The EPR spectra were collected on Bruker EMX Plus with microwave frequency of 9.82 GHz, microwave power of 2.0 mW, modulation frequency of 100 kHz, modulation amplitude of 0.8 G, sweep width of 120 G and sweep time of 30 s.

DATA AVAILABILITY

The data supporting the findings of this study are available within the paper and its Supplementary Information file.

Received: 22 April 2023; Accepted: 20 October 2023;
Published online: 01 November 2023

REFERENCES

1. Lashgari, M., Naseri-Moghanlou, S., Khanahmadlou, T. & Hempelmann, R. Electrostatic boosting of ionic dye pollutant removal from aquatic environment using a single electrode photoreactor. *npj Clean Water* **6**, 10 (2023).
2. Ribeiro, R. S. et al. Catalytic wet peroxide oxidation: a route towards the application of hybrid magnetic carbon nanocomposites for the degradation of organic pollutants. A review. *Appl. Catal. B: Environ.* **187**, 428–460 (2016).
3. Munoz, M., de Pedro, Z. M., Casas, J. A. & Rodriguez, J. J. Preparation of magnetite-based catalysts and their application in heterogeneous Fenton oxidation – A review. *Appl. Catal. B: Environ.* **176-177**, 249–265 (2015).
4. Guo, S. et al. Three-dimensionally printed zero-valent copper with hierarchically porous structures as an efficient Fenton-like catalyst for enhanced degradation of tetracycline. *Catalysts* **13**, 446 (2023).
5. Kim, Y., Marcano, M. C., Kim, S. & Becker, U. Reduction of uranyl and uranyl-organic complexes mediated by magnetite and ilmenite: A combined electrochemical AFM and DFT study. *Geochim. Cosmochim. Ac.* **293**, 127–141 (2021).
6. Dhineshbabu, N. R. & Bose, S. UV resistant and fire retardant properties in fabrics coated with polymer based nanocomposites derived from sustainable and natural resources for protective clothing application. *Composites Part B: Engineering* **172**, 555–563 (2019).
7. Dhineshbabu, N. R. & Bose, S. Smart textiles coated with eco-friendly UV-blocking nanoparticles derived from natural resources. *ACS Omega* **3**, 7454–7465 (2018).
8. Torres-Luna, J. A., Sanabria, N. R. & Carriazo, J. G. Powders of iron(III)-doped titanium dioxide obtained by direct way from a natural ilmenite. *Powder Technol.* **302**, 254–260 (2016).
9. Li, Z., Wang, Z. & Li, G. Preparation of nano-titanium dioxide from ilmenite using sulfuric acid-decomposition by liquid phase method. *Powder Technol.* **287**, 256–263 (2016).
10. Wei, J., Han, D., Bi, J. & Gong, J. Fe-doped ilmenite $CoTiO_3$ for antibiotic removal: Electronic modulation and enhanced activation of peroxymonosulfate. *Chem. Eng. J.* **423**, 130165 (2021).
11. Sekar, S. et al. Excellent nitroarene reduction activity of ilmenite nanochips prepared by facile template-free hydrothermal synthesis. *Ceram. Int.* **48**, 29421–29428 (2022).
12. García-Muñoz, P. et al. Ilmenite ($FeTiO_3$) as low cost catalyst for advanced oxidation processes. *J. Environ. Chem. Eng.* **4**, 542–548 (2016).
13. García-Muñoz, P. et al. Modified ilmenite as catalyst for CWPO-photoassisted process under LED light. *Chem. Eng. J.* **318**, 89–94 (2017).
14. Chen, F., Xie, S., Huang, X. & Qiu, X. Ionothermal synthesis of Fe_3O_4 magnetic nanoparticles as efficient heterogeneous Fenton-like catalysts for degradation of organic pollutants with H_2O_2. *J. Hazard. Mater.* **322**, 152–162 (2017).
15. Huang, X., Xu, C., Ma, J. & Chen, F. Ionothermal synthesis of Cu-doped Fe_3O_4 magnetic nanoparticles with enhanced peroxidase-like activity for organic wastewater treatment. *Adv. Powder Technol.* **29**, 796–803 (2018).
16. Chen, W., Zhang, J. & Chen, F. Glycothermal synthesis of fluorinated Fe_3O_4 microspheres with distinct peroxidase-like activity. *Adv. Powder Technol.* **30**, 999–1005 (2019).
17. Zhang, J., Wang, Z., Chen, R. & Chen, F. New soft chemistry route to titano-magnetite magnetic nanoparticles with enhanced peroxidase-like activity. *Powder Technol.* **373**, 39–45 (2020).
18. Du, W. et al. Copper-promoted heterogeneous Fenton-like oxidation of Rhodamine B over Fe_3O_4 magnetic nanocatalysts at mild conditions. *Environ. Sci. Pollut. Res.* **28**, 19959–19968 (2021).

19. Chen, F., Lv, H., Chen, W. & Chen, R. Catalytic wet peroxide oxidation of anionic pollutants over fluorinated Fe_3O_4 microspheres at circumneutral pH values. *Catalysts* **12**, 1564 (2022).
20. Teel, A. L. et al. Rates of trace mineral-catalyzed decomposition of hydrogen peroxide. *J. Environ. Eng.* **133**, 853–858 (2007).
21. Zarazua-Morin, M. E. et al. Synthesis, characterization, and catalytic activity of $FeTiO_3/TiO_2$ for photodegradation of organic pollutants with visible light. *Res. Chem. Intermediat.* **42**, 1029–1043 (2016).
22. Yong, J. K. et al. Heterojunction of $FeTiO_3$ nanodisc and TiO_2 nanoparticle for a novel visible light photocatalyst*J. Phys. Chem. C* **113**, 19179–19184 (2009).
23. Liu, Y. et al. Synthesis and non-isothermal carbothermic reduction of $FeTiO_3$-Fe_2O_3 solid solution systems. *Metallurgical Mater. Transact. B* **48**, 2419–2427 (2017).
24. Shi, J. et al. Ferromagetic-paramagnetic transformation in hydrogenated ferrous titanate. *Ceram. Int.* **46**, 5360–5367 (2020).
25. Guan, X.-F. et al. Synthesis of $FeTiO_3$ nanosheets with {0001} facets exposed: enhanced electrochemical performance and catalytic activity. *RSC Adv.* **3**, 13635 (2013).
26. Gambhire, A. B. et al. Synthesis and characterization of $FeTiO_3$ ceramics. *Arab J. Chem.* **9**, S429–S432 (2016).
27. Raghavender, A. T. et al. Nano-ilmenite $FeTiO_3$: Synthesis and characterization, J. Magn. Magn. *Mater.* **331**, 129–132 (2013).
28. Chen, Y. H. Synthesis, characterization and dye adsorption of ilmenite nanoparticles. *J. Non-cryst. Solids.* **357**, 136–139 (2011).
29. Kresge, C. T. et al. Ordered mesoporous molecular sieves synthesized by a liquid-crystal template mechanism. *Nature* **359**, 710–712 (1992).
30. Said, S., Aman, D., Riad, M. & Mikhail, S. MoZn/AlPO4-5 zeolite: Preparation, structural characterization and catalytic dehydration of ethanol. *J. Solid State Chem.* **287**, 10 (2020).
31. Du, J. P. et al. Investigation of suitable templates for one-pot-synthesized Cu-SAPO-34 in NOx abatement from diesel vehicle exhaust. *Environ. Sci. Technol.* **54**, 7870–7878 (2020).
32. Doan, T. et al. Zeotype SAPO-34 Synthesized by Combination of Templates for the Gasification of Biomass. *Chem. Eng. Technol.* **43**, 731–741 (2020).
33. Luo, Z. R. et al. Triethylamine-templated nanocalix Ln(12) clusters of diacylhydrazone: crystal structures and magnetic properties. *Dalton Trans.* **48**, 17414–17421 (2019).
34. Pan, Y. Y. et al. Efficient post-synthesis of hierarchical SAPO-34 zeolites via organic amine etching under hydrothermal conditions and their enhanced MTO performance. *Inorg. Chem. Front.* **6**, 1299–1303 (2019).
35. Zhang, N. et al. Lanthanide hydroxide nanorods and their thermal decomposition to lanthanide oxide nanorods. *Mater. Chem. Phys.* **114**, 160–167 (2009).
36. YI, R. et al. Large-scale hydrothermal synthesis and characterization of size-controlled lanthanum hydroxide nanorods. *Chin. J. Chem.* **27**, 920–924 (2009).
37. Lv, W. et al. Carbothermic reduction of ilmenite concentrate in semi-molten state by adding sodium sulfate. *Powder Technol.* **340**, 354–361 (2018).
38. Harrison, R. J., Redfern, S. A. T. & Smith, R. I. In-situ study of the $R\bar{3}$ to $R\bar{3}c$ phase transition in the ilmenite-hematite solid solution using time-of-flight neutron powder diffraction. *Am. Mineral.* **85,** 194–205 (2000).
39. Jiang, H. et al. Defect-rich and ultrathin N doped carbon nanosheets as advanced trifunctional metal-free electrocatalysts for the ORR, OER and HER, Energ. *Environ. Sci.* **12**, 322–333 (2019).
40. Chen, G. et al. Promoted oxygen reduction kinetics on nitrogen-doped hierarchically porous carbon by engineering proton-feeding centers, Energ. *Environ. Sci.* **13**, 2849–2855 (2020).
41. Li, X., Guan, B. Y., Gao, S. & Lou, X. W. A general dual-templating approach to biomass-derived hierarchically porous heteroatom-doped carbon materials for enhanced electrocatalytic oxygen reduction, Energ. *Environ. Sci.* **12**, 648–655 (2019).
42. Zeng, T. et al. Synergistically enhancing Fenton-like degradation of organics by in situ transformation from Fe_3O_4 microspheres to mesoporous Fe, N-dual doped carbon. *Sci. Total Environ.* **645**, 550–559 (2018).
43. Wang, J. H. et al. An ultrafast and facile nondestructive strategy to convert various inefficient commercial nanocarbons to highly active Fenton-like catalysts, P. *Natl. Acad. Sci. USA.* **119**, e2114138119 (2022).
44. Han, T. et al. Hierarchical $FeTiO_3$-TiO_2 hollow spheres for efficient simulated sunlight-driven water oxidation. *Nanoscale* **7**, 15924–15934 (2015).
45. Aparna, T. K. & Sivasubramanian, R. $FeTiO_3$ nanohexagons based electrochemical sensor for the detection of dopamine in presence of uric acid. *Mater. Chem. Phys.* **233**, 319–328 (2019).
46. Guo, S. et al. Enhancing electrochemical performances of TiO_2 porous microspheres through hybridizing with $FeTiO_3$ and nanocarbon. *Electrochim. Acta* **190**, 556–565 (2016).
47. Zhang, Q. et al. Synthesis of $SrFe_xTi_{1-x}O_{3-\delta}$ nanocubes with tunable oxygen vacancies for selective and efficient photocatalytic NO oxidation. *Appl. Catal. B: Environ.* **239**, 1–9 (2018).
48. Zhou, Y. et al. Self-assembled iron-containing mordenite monolith for carbon dioxide sieving. *Science* **373**, 315–320 (2021).
49. Lari, G. M., Mondelli, C., Pérez-Ramírez, J. Gas-phase oxidation of glycerol to dihydroxyacetone over tailored iron zeolites, *ACS Catal.* **5**, 1453–14461 (2015).
50. Yamashita, T. & Hayes, P. Analysis of XPS spectra of Fe^{2+} and Fe^{3+} ions in oxide materials. *Appl. Surf. Sci.* **254**, 2441–2449 (2008).
51. Sha, S.-C. et al. Cation−π interactions in the benzylic arylation of toluenes with bimetallic catalysts, J. Am. *Chem. Soc.* **140**, 12415–12423 (2018).
52. Neel, A. J., Hilton, M. J., Sigman, M. S. & Toste, F. D. Exploiting non-covalent π interactions for catalyst design. *Nature* **543**, 637–646 (2017).
53. Park, S. et al. Cation−π interactions contribute to hydrophobic humic acid removal for the control of hydraulically irreversible membrane fouling. *Environ. Sci. Technol.* **57**, 3853–3863 (2023).
54. Matta, R., Hanna, K. & Chiron, S. Fenton-like oxidation of 2,4,6-trinitrotoluene using different iron minerals. *Sci. Total Environ.* **385**, 242–251 (2007).
55. Chen, Y., Miller, C. J., Collins, R. N. & Waite, T. D. Key considerations when assessing novel Fenton catalysts: Iron oxychloride (FeOCl) as a case study. *Environ. Sci. Technol.* **55**, 13317–13325 (2021).
56. Yang, S. et al. Degradation efficiencies of azo dye Acid Orange 7 by the interaction of heat, UV and anions with common oxidants: Persulfate, peroxymonosulfate and hydrogen peroxide. *J. Hazard. Mater.* **179**, 552–558 (2010).
57. Fan, Y. et al. Kinetic and mechanistic investigations of the degradation of sulfamethazine in heat-activated persulfate oxidation process. *J. Hazard. Mater.* **300**, 39–47 (2015).
58. Duan, X. et al. Occurrence of radical and nonradical pathways from carbocatalysts for aqueous and nonaqueous catalytic oxidation. *Appl. Catal. B: Environ.* **188**, 98–105 (2016).
59. Qi, C. et al. Activation of peroxymonosulfate by base: Implications for the degradation of organic pollutants. *Chemosphere* **151**, 280–288 (2016).
60. Chen, C. et al. In-situ pyrolysis of Enteromorpha as carbocatalyst for catalytic removal of organic contaminants: Considering the intrinsic N/Fe in Enteromorpha and non-radical reaction. *Appl. Catal. B: Environ.* **250**, 382–395 (2019).
61. Long, Y. et al. Peroxymonosulfate activation for pollutants degradation by Fe-N-codoped carbonaceous catalyst: Structure-dependent performance and mechanism insight. *Chem. Eng. J.* **369**, 542–552 (2019).
62. Chen, F., Zhao, J. & Hidaka, H. Highly selective deethylation of rhodamine B: Adsorption and photooxidation pathways of the dye on the TiO_2/SiO_2 composite photocatalyst. *Int. J. Photoenergy.* **5**, 209–217 (2003).
63. He, Z. et al. Photocatalytic degradation of rhodamine B by Bi_2WO_6 with electron accepting agent under microwave irradiation: mechanism and pathway. *J. Hazard. Mater.* **162**, 1477–1486 (2009).
64. Shirani, Z., Santhosh, C., Iqbal, J. & Bhatnagar, A. Waste Moringa oleifera seed pods as green sorbent for efficient removal of toxic aquatic pollutants. *J. Environ. Manage.* **227**, 95–106 (2018).
65. Sepehr, M. N. et al. Adsorption performance of magnesium/aluminum layered double hydroxide nanoparticles for metronidazole from aqueous solution. *Arab. J. Chem.* **10**, 611–623 (2016).

ACKNOWLEDGEMENTS

This work was supported by National Natural Science Foundation of China (No. 52370086) and Innovative Team Program of Natural Science Foundation of Hubei Province (Grant No. 2023AFA027).

AUTHOR CONTRIBUTIONS

S.G.: Investigation and writing-original draft. R.H.: Investigation and methodology. J.Y.: Investigation. R.C.: Resources. F.C.: Conceptualization, resources, supervision, writing-review & editing. All the authors have read and approved the paper.

COMPETING INTERESTS

The authors declare no competing interests.

ADDITIONAL INFORMATION

Supplementary information The online version contains supplementary material available at https://doi.org/10.1038/s41545-023-00287-1.

Correspondence and requests for materials should be addressed to Fengxi Chen.

Reprints and permission information is available at http://www.nature.com/reprints

Publisher's note Springer Nature remains neutral with regard to jurisdictional claims in published maps and institutional affiliations.